Monthly Notices
of th

the Eddington ratio is extremely high, $0.83 < L_{bol}/L_{Edd} < 2.56$. Even considering possible more polar line-of-sight effects in the black hole mass estimate, one concludes that the Eddington ratio is $\gtrsim 100$ per cent. This seems very extreme, so one must also ask if there is a significant contribution to the continuum from the optical high-frequency tail of the synchrotron emission associated with the radio core? There are two strong pieces of evidence against this possibility. First of all, the optical polarization is very low, 0.5 per cent, which is atypical of blazar dilution of the optical quasar spectrum in low-redshift sources (Wills et al. 1992). Secondly, the EUV spectrum in Fig. 1 shows very strong emission lines for which the equivalent width does not appear to be reduced by a synchrotron background component. Super-Eddington accretion rates were previously found by the completely independent method of fitting accretion disc models to the broad-band spectrum (Malkan 1983). PKS 0405−123, with its powerful radio lobes (see the next section), is perhaps the most extreme counter example to the notion that RLQs are associated with low Eddington rates (Borozdin 2002). This is apparently a very remarkable radio source worthy of further detailed study. The EUV continuum fit is indicated by the dashed red line and it is estimated that $L_{EUV} = 1.80$.

2.3 3C 57

3C 57 is a luminous quasar at $z = 0.671$ with a complex radio morphology. It has a double steep spectrum nucleus (two bright components separated by 9 kpc, located within the host galaxy) and a low-luminosity radio lobe (Hutchings, Price & Gower 1988; Reid, Kronberg & Perley 1999). This cryptic radio structure will be analysed in detail in the next section. The results in Table 1 indicate a range of virial central black hole mass estimates, $7 \times 10^8\ M_\odot < M_{bh} < 9.3 \times 10^8\ M_\odot$. The quasar was observed on 2011 August 17 with the G160M grating and on 2011 August 19 with the G130M grating. These data were downloaded from MAST.

In the bottom frame of Fig. 1, the EUV spectrum corrected for Galactic extinction using the method of Cardelli et al. (1989) with $R_V = 3.1$, and the visual extinction from NED is plotted. Equation (1) and the spectrum in Fig. 1 indicate a high luminosity, $L_{bol} \simeq 8.2 \times 10^{46}$ erg s^{-1}. From the black hole mass estimate, the Eddington ratio is extremely high, $L_{bol}/L_{Edd} \simeq 0.81 \pm 0.11$. The EUV continuum fit is indicated by the dashed red line and it is estimated that $L_{EUV} = 1.65$. An attempt was made to consider the possibility that the decline in the flux density at wavelengths just above the excised Galactic Lyα region is a consequence of a Lyman limit system (at approximately with $\lambda_o \simeq 1235$ Å) as was done for 3C 95. In this scenario, even a 15–20 per cent decrement correction degraded the continuum extension significantly from just above the excised Galactic Lyα region of the spectrum to that below the excised Galactic Lyα region of the spectrum. Any Lyman limit system correction will raise the continuum at wavelengths just above the excised Galactic Lyα region of the spectrum more than it will below the excised region. This exaggerates the already existing small dip in the continuum in this region (see Fig. 1), making the continuum look very unnatural. It is concluded that the decline in the flux density at the short wavelength end of the spectrum relative to the flux density at wavelengths just above the excised Galactic Lyα region represents the expected drop in the emission line flux shortward of the blue wing of the very broad blend of N V, Ne VIII and O IV that is generally very strong in all of the spectra in Fig.

3 ESTIMATING THE LONG-TERM TIME-AVERAGED JET POWER

A method that allows one to convert 151 MHz flux densities, F_{151} (measured in Jy), into estimates of long-term time-averaged jet power, $\overline{Q}$, (measured in erg s^{-1}) is captured by the formula derived in Willott et al. (1999) and Punsly (2005):

$$\overline{Q} \simeq [(f/15)^{3/2}]1.1 \times 10^{45} \left[X^{1+}\, Z^2 F_{151}\right]^{0.857} \mathrm{erg\ s^{-1}}, \quad (2)$$

$$Z \simeq 3.31 - (3.65) \times \left[X^4 - 0.203X^3 + 0.749X^2 + 0.444X + 0.205\right]^{-0.125}, \quad (3)$$

where $X = 1 + z$, F_{151} is the total optically thin flux density from the lobes (i.e. contributions from Doppler-boosted jets or radio cores are removed). This calculation of the jet kinetic luminosity incorporates deviations from the overly simplified minimum energy estimates into a multiplicative factor, f that represents the small departures from minimum energy, geometric effects, filling factors, protonic contributions and low-frequency cutoff (Willott et al. 1999). The quantity, f, was further determined to most likely be in the range of 10–20 (Blundell & Rawlings 2000). In this paper, we adopt the following cosmological parameters: $H_0 = 70$ km s^{-1} Mpc^{-1}, $= 0.7$ and $_m = 0.3$. Define the radio spectral index, α as F . The formula is most accurate for large classical double radio sources, thus, we do not consider sources with a linear size of less than 20 kpc, which are constrained by the ambient pressure of the host galaxy. Alternatively, one can also use the independently derived isotropic estimator in which the lobe energy is primarily inertial in form (Punsly 2005):

$$\overline{Q} \simeq 5.7 \times 10^{44}(1+z)^{1+}\, Z^2 F_{151}\ \mathrm{erg\ s^{-1}}. \quad (4)$$

Due to Doppler boosting on kpc scales, core-dominated sources with a very bright one-sided jet (such as 3C 279 and most blazars) must be treated with care (Punsly 1995). The best estimate is to take the lobe-flux density on the counter-jet side and multiply this value by 2 (bilateral symmetry assumption) and use this estimate for the flux density in equations (2) and (4).

For strong radio sources, the value of equation (4) is typically slightly less than that found in equation (3) with $f = 10$ (Punsly 2005). Thus, we take equation (4) as a lower bound on the estimate of $\overline{Q}$ (Blundell & Rawlings 2000). Likewise, equation (2) with $f = 20$ is the maximum upper bound on the estimate of $\overline{Q}$ in the following (Willott et al. 1999; Blundell & Rawlings 2000). The values of $\overline{Q}$ that we list below are the average of the upper and lower bound. The assigned uncertainty is the difference between the maximum bound and the average.

3C 95 is a large lobe-dominated quasar, so the 24.8 Jy of flux at 160 MHz found in NED is due almost entirely from the radio lobes. A typical lobe spectral index of -0.8 and equations (2)–(4) indicate that $\overline{Q} = 1.6 \pm 0.5 \times 10^{46}$. PKS 0405−123 has a strong flat spectrum radio core. The multifrequency component decomposition from Hutchings et al. (1996) is used to subtract off the core flux density as a function of wavelength. The lobe flux density is 1580 mJy at 1.41 GHz. Using -0.8 and equations (2)–(4) indicates that $\overline{Q} = 8.1 \pm 3.0 \times 10^{45}$ erg s^{-1}.

As mentioned earlier, the radio morphology of 3C 57 is more complicated. Fig. 2 is a previously unpublished radio image of 3C 57 at 1.52 GHz from the Very Large Array (VLA) in A-Array from 1988 October 31. The spatial resolution is reasonably well matched to published VLA B-array at 4.86 GHz observations and the VLA C-array observations at 14.94 GHz (Bogers et al. 1994; Reid et al.

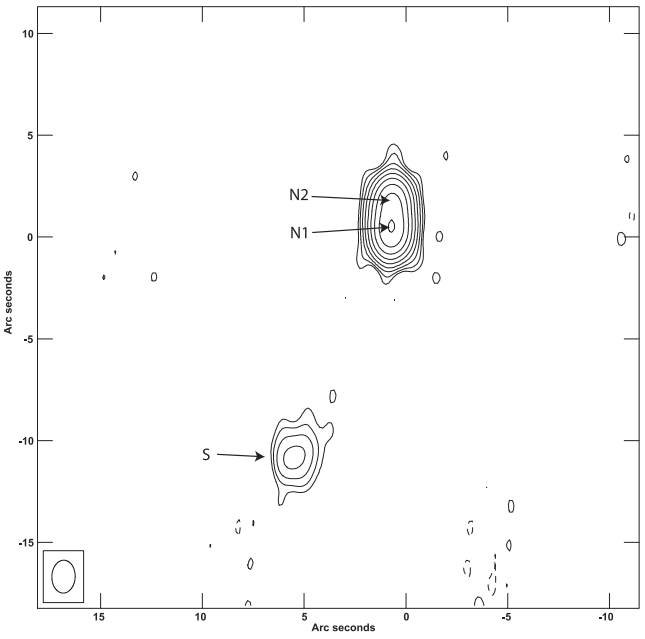

Figure 2. A VLA radio image of 3C 57 at 1.5 GHz. Note the lobe emission to the southeast and the partially resolved northern component. The northern component is fit by two elliptical Gaussian models, denoted by N1 and N2, separated by 1.35 arcsec. The contours start at 6.6 mJy beam^{-1} and increase in factors of 2 to a maximum of 1690 mJy beam^{-1}.

). We have captured the results of a three-component model of the source at the three frequencies in Table 2. The components are a southern lobe and a northern component that we split as N1 and N2. The northern component is partially resolved, and is fit by two elliptical Gaussians separated by 1.35 arcsec. The columns (2)–(5) list the frequency of observation, the beamwidth, the rms noise level and the flux densities for each component in the model. The matched resolution allows us to estimate the spectral index of the components in a two-component fit to the northern component. The spectral indices are derived from the best fit to the three data points for each component and are tabulated in the last column. Component N1 is more luminous above 1 GHz and is flatter spectrum. This is likely the true nucleus. The spectral index for the lobe is not reliable. The flux densities at 4.86 and 14.94 GHz are not reliable for a diffuse lobe, since the surface brightness is very low for this steep-spectrum feature. Typically, flux is missed in higher frequency observations of diffuse low-surface brightness structures. Thus, we still cannot rule out a more typical spectral index of $\alpha = -0.8$ for the lobe emission.

The first thing that we analyse is component N1. We have three reliable flux density measurements. We note that this component dominates the spectrum at 14.94 GHz and the spectrum is the flattest of the three components. Therefore, it should comprise the preponderance of flux at 90 GHz. The flux density at 90 GHz is 280 ± 60 mJy (Steppe et al. 1988). In addition to the three values in Table 2, 90 GHz provides a fourth frequency for which the flux density is captured. The data in Table 1 already indicates a spectral break at 4.86 GHz. So, we fit these four points with a model comprised of two power laws. There will be two amplitudes and two power-law indices representing four equations (the total flux at each of the four frequencies) and four unknowns (the four parameters of the two-component model), so there exists a solution if the model is a good approximation to the data. Based on many other steep spectrum radio cores, one expects that a flat spectrum core might be buried inside this feature. The left-hand frame of Fig. 3 is our two-component fit. We describe the optically thin (steep) component of N1 by a flux density at 4.86 GHz of 339 mJy and a power-law spectral index of 0.97. We describe the optically thick (flat) component of N1 by a flux density at 4.86 GHz of 431 mJy and a power-law spectral index of 0.18. This analysis clearly identifies N1 with the central engine and the true nucleus.

An identification and characterization of the nucleus elucidates the nature of the triple radio source in Fig. 2. The right frame of Fig. 3 compares a four-power-law-component model to the radio data from NED augmented by the 90 GHz data and we correct the 31.4 GHz data from NED, it should be 530 ± 120 mJy (Geldzahler & Witzel 1981). The four-component model is the two-power-law-component model of N1 (from the left-hand frame) and the power law for N2 in Table 2 and the radio lobe with a spectral index $\alpha = -0.8$ and 106 mJy at 1.52 GHz. The sum of the four components is the dark black curve. The curve fits the data very well from 750 MHz to 90 GHz. Below 750 MHz, the flux density of the model starts to exceed the actual data significantly. Below 750 MHz, there is clearly a spectral break required to fit the low-frequency spectrum. This is likely a consequence free–free absorption, a phenomenon commonly attributed to the spectral turnover of gigahertz peaked radio sources (O'Dea 1998). We also note a small discrepancy in the fit near 20 GHz. This might be evidence of blazar-like variability of the flat spectrum radio core.

One can compute the total radio luminosity of the compact steep spectrum regions, if one assumes a strong spectral break between 365 and 750 MHz based on the right-hand frame of Fig. 3. Secondly, we assume that spectral ageing creates an enhanced downward curvature in the spectrum at 50 GHz. The radio luminosity, L_{radio} is $2.3 \pm 0.2 \times 10^{44}$ erg s^{-1} for the steep spectrum component of N1 and $2.6 \pm 0.2 \times 10^{44}$ erg s^{-1} for the northern component of the compact double.

The radio lobe 65 kpc to the southeast shows faint extensions and an elongation back towards the nuclear region. This is indicative of a hotspot at the termination of a radio jet. Higher sensitivity 1.4 GHz B-Array observations with the VLA might reveal some extended jet-like emission in this region. Comparing the flux density

Table 2. Summary of VLA observations of the components of 3C57.

Component	1.52 GHz Flux Density (mJy) 1.6 arcsec beamwidth rms = 0.8 mJy beam^{-1} 1988/10/31	4.86 GHz Flux Density (mJy)/ 1.8 arcsec beamwidth rms = 0.4 mJy beam^{-1} 1989/3/18	14.94 Flux Density (mJy) 1.9 arcsec beamwidth rms = 0.8 mJy beam^{-1} 1987/1/12	
Component N2	1076 ± 55	381 ± 11	155 ± 5	0.87
Component N1	1590 ± 80	765 ± 22	476 ± 15	0.54
Southern lobe, S	106 ± 6	29 ± 2	9 ± 1	1.07

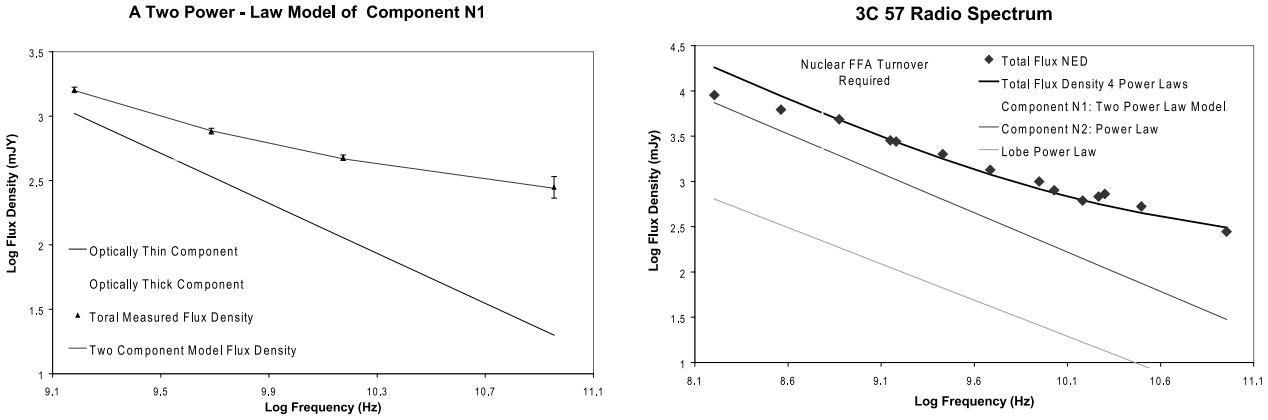

Figure 3. The left frame shows that the two-power-law-component model represents the four spectral data points of the component N1 from Table 1 and is constrained by the 90 GHz flux density from Steppe et al. (). The right frame synthesizes the two-power-law-component model of component N1, the power law for component N2 in Table 1 and the radio lobe with a spectral index $\alpha = 0.8$ and 106 mJy at 1.52 GHz in order to facilitate a comparison to the observed data. This is a four-component model and the sum of the four components is the dark black curve. The curve fits the data very well from 750 MHz to 90 GHz. Below 750 MHz there is clearly a spectral break required to fit the low-frequency spectrum. This is typically due to free–free absorption (FFA).

of the faint radio lobe from 1.5, 5 and 15 GHz indicates a very steep spectrum with > 1. As noted above, this result is likely skewed by faint diffuse emission being resolved out at high frequency. However, a very steep spectrum is not ruled out. In order to capture this possibility, we extrapolate the 1.52 GHz flux density of 106 mJy to 151 MHz (required for equations 2 and 4) two different ways. For the upper bound from equation (2), we choose $= 1$ and for the lower bound in equation (4), we use a more conventional $= 0.8$. A 300 MHz VLA A-array observation would resolve this ambiguity. However, as noted in the discussion below equation (4), we need to multiply our calculation of $\overline{Q}$ by 2 in order to account for the lack of an estimate for the northern radio jet. The northern radio jet (component N2) is apparently thwarted by galactic gas and dissipates 9 kpc from the nucleus. Thus we estimate $\overline{Q} = 1.4 \pm 0.7 \times 10^{45}$ erg s^{-1}. In this interpretation, and noting the value of L_{radio}, above, the northern jet dissipates between 21 per cent and 76 per cent of its energy as radio emission on sub-galactic scales in component N2.

The large dissipation of jet power into radio luminosity is not entirely unexpected. Recall the comment in the text following equation (3). Our estimators of jet power in equations (2) and (4) are technically accurate only for relaxed classical double radio sources. These radio sources expand into a diffuse intragalactic medium. Hence, our restriction of applicability that the lobe must be $\gtrsim 20$ kpc from the central engine (outside of the host galaxy) in order for us to apply this relationship to our radio sources. Equation (2) yields a radio luminosity $\lesssim 1$ per cent of the jet power. A similar result has been found for in studies of classical relaxed radio sources (Cavagnolo et al. 2010; Daly et al. 2012). Component N2 is 9 kpc from the central engine, and as we have noted previously, it is likely located within the dense medium of the host galaxy. The work required to displace dense nebular clouds and the intergalactic medium, in general, likely involves magnetohydrodynamic waves (including shock waves) and instabilities that can be highly dissipative. This leads to an enhanced radiative luminosity and equations (2) and (3) will always drastically overestimate the power of the jet if the enveloping environment is dense. However, in the context of the large radio luminosity of the northern component noted above, this does not preclude the possibility that the central engine underwent 'a brief' (relative to the long lifetime of the radio source) episode of elevated jet power 30 000 yr ago.

4 DISCUSSION

This paper considers the EUV spectrum and radio properties of three RLQs at the high-end region of the quasar L_{bol}/L_{Edd} parameter space. In the left-hand frame of Fig. 4 is the scatter plot of $\overline{Q}/L_{bol}$ – $_{EUV}$ from Punsly & Marziani (2015) with our three new sources added. The three quasars conform to the existing correlation. The exploration of the high end of L_{bol}/L_{Edd} parameter space can be used to fortify the statistics of the partial correlation analysis of Punsly (2015) amongst the variables $\overline{Q}/L_{bol}$, $\overline{Q}$ and $_{EUV}$ that indicated that the correlation of $\overline{Q}/L_{bol}$ and $_{EUV}$ is fundamental and the correlation of $\overline{Q}$ and $_{EUV}$ is spurious. In particular, consider the Spearman partial correlation of $\overline{Q}/L_{bol}$ with $_{EUV}$ when $\overline{Q}$ is held fixed. The partial correlation coefficient with the expanded sample is 0.594 (was 0.492 in Punsly 2015), which corresponds to a statistical significance of 0.998 (was 0.984). Conversely, the partial correlation of $\overline{Q}$ with $_{EUV}$, when $\overline{Q}/L_{bol}$ is held fixed has a statistical significance of only 0.188 (was 0.581). Thus, the addition of quasars from the high end of L_{bol}/L_{Edd} parameter space to the sample has accentuated the fact that the correlation of $\overline{Q}/L_{bol}$ and $_{EUV}$ is fundamental and the correlation of $\overline{Q}$ and $_{EUV}$ is spurious at a very high statistical significance level.

This is a very important result at a fundamental physical level. For example, it highlights the fact that the mass accretion rate is strongly coupled to jet power in quasars that can support a relativistic jet. In particular, the accretion rate regulates jet power in RLQs. As discussed in detail in Punsly (2015), this is a basic prediction of magnetically arrested accretion scenarios for jet production in quasars. This idea is predicated on the fact that large-scale magnetic flux is trapped within the inner accretion flow by ram pressure. The rotating magnetic flux is the source of the relativistic jet. More trapped magnetic flux means a stronger jet. The trapped poloidal magnetic flux is vertical as it penetrates the inner accretion flow (perpendicular to the plane on the inflow) in some numerical simulations and models of magnetically arrested accretion (Igumenshchev 2008; Punsly, Igumenshchev & Hirose 2009).

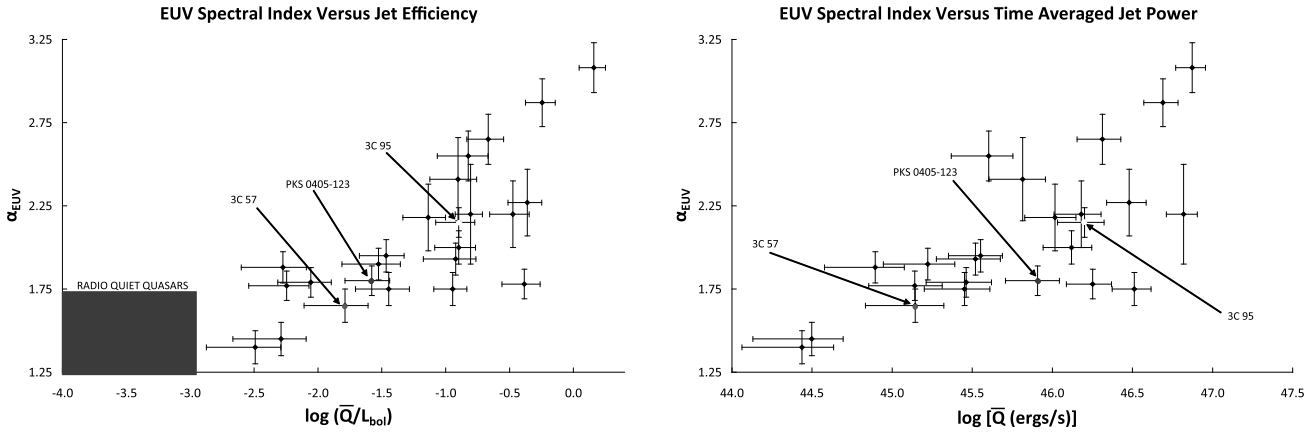

Figure 4. A comparison of the scatter of the correlation of the EUV spectral index, α_{EUV}, with time-averaged jet power $\overline{Q}$ (on the right), and the scatter of the correlation of α_{EUV} with the time-averaged jet power normalized by the bolometric luminosity of the accretion flow, $\overline{Q}/L_{bol}$ (on the left). These plots help to visualize the partial correlation analysis described in the text. Normalizing by the bolometric luminosity reduces the scatter at a very high statistical signi cance.

Thus, as the large-scale magnetic ux forms the base of the radio jet, the thermal gas that is displaced by the magnetic ux results in less EUV emission from the inner accretion ow. Thus, a consistent explanation of the $\overline{Q}/L_{bol}$ and α_{EUV} correlation is achieved given that there is signi cant vertical ux that threads the inner accretion ow.

ACKNOWLEDGEMENTS

BP acknowledges support from ICRANet.

REFERENCES

Blundell K., Rawlings S., 2000, AJ, 119, 1111
Bogers W., Hes R., Barthel P. D., Zensus J. A., 1994, A&A, 105, 91
Boroson T., 2002, ApJ, 565 78
Cardelli J., Clayton G., Mathis J., 1989, ApJ, 345, 245
Cavagnolo K., McNamara B., Nulsen J., Carilli C., Jones C., Birzan L., 2010, ApJ, 720, 1066
Daly R., Sprinkle T., O'Dea C., Kharb P., Baum S., 2012, MNRAS, 423, 2498
Davis S., Laor A., 2011, ApJ, 728, 98
Decarli R., Dotti M., Treves A., 2011, MNRAS, 413, 39
Geldzahler B., Witzel A., 1981, AJ, 86, 1306
Hutchings J., Price E., Gower A., 1988, ApJ, 329, 122
Hutchings J., Gower A., Reynveld S., Dewey A., 1996, AJ, 111, 2167
Igumenshchev I. V., 2008, ApJ, 677, 317
Malkan M., 1983, ApJ, 268, 582
Marziani P., Sulentic J. W., Zamanov R., Calvani M., Dultzin-Hacyan D., Bachev R., Zwitter T., 2003, ApJS, 145, 199
O'Dea C., 1998, PASP, 110, 493
Price E., Gower A., Hutchings J., Talon S., Duncan D., Ross G., 1993, ApJS, 86, 365
Punsly B., 1995, AJ, 109, 1555
Punsly B., 2005, ApJ, 623, L9
Punsly B., 2014, ApJ, 797, L33
Punsly B., 2015, ApJ, 806, 47
Punsly B., Marziani P., 2015, MNRAS, 453, L16
Punsly B., Igumenshchev I. V., Hirose S., 2009, ApJ, 704, 1065
Punsly B., Marziani P., Kharb P., O'Dea C., Vestergaard M., 2016, ApJ, 812, 79
Reid R. I., Kronberg P. P., Perley R. A., 1999, ApJS, 124, 285
Shen Y., Liu X., 2012, ApJ, 753, 125
Shull M., Stevans M., Danforth C., 2012, ApJ, 752, 162
Steppe H., Salter C. J., Chini R., Kreysa E., Brunswig W., Lobato P. J., 1988, A&AS, 75, 317
Sulentic J., Marziani P., del Olmo A., Stirpe G. M., Zamanov R., Plauchu-Frayn I., 2015, MNRAS, 450, 1916
Telfer R., Zheng W., Kriss G., Davidsen A., 2002, ApJ, 565, 773
Vestergaard M., Peterson B., 2006, ApJ, 641, 689
Willott C., Rawlings S., Blundell K., Lacy M., 1999, MNRAS, 309, 1017
Wills B. J., Wills D., Breger M., Antonucci R., Barvainis R., 1992, ApJ, 398, 454
Zheng W., Kriss G. A., Telfer R. C., Grimes J. P., Davidsen A. F., 1997, ApJ, 475, 469

This paper has been typeset from a TEX/LATEX file prepared by the author.